

**Supplementary Information:**

**Origins of pressure-induced enhancement in thermal conductivity of hybrid organic-inorganic perovskite**

Ashutosh Giri<sup>1, a)</sup>

*Department of Mechanical, Industrial and Systems Engineering,  
University of Rhode Island, Kingston, RI 02881, USA*

---

<sup>a)</sup>Electronic mail: ashgiri@uri.edu

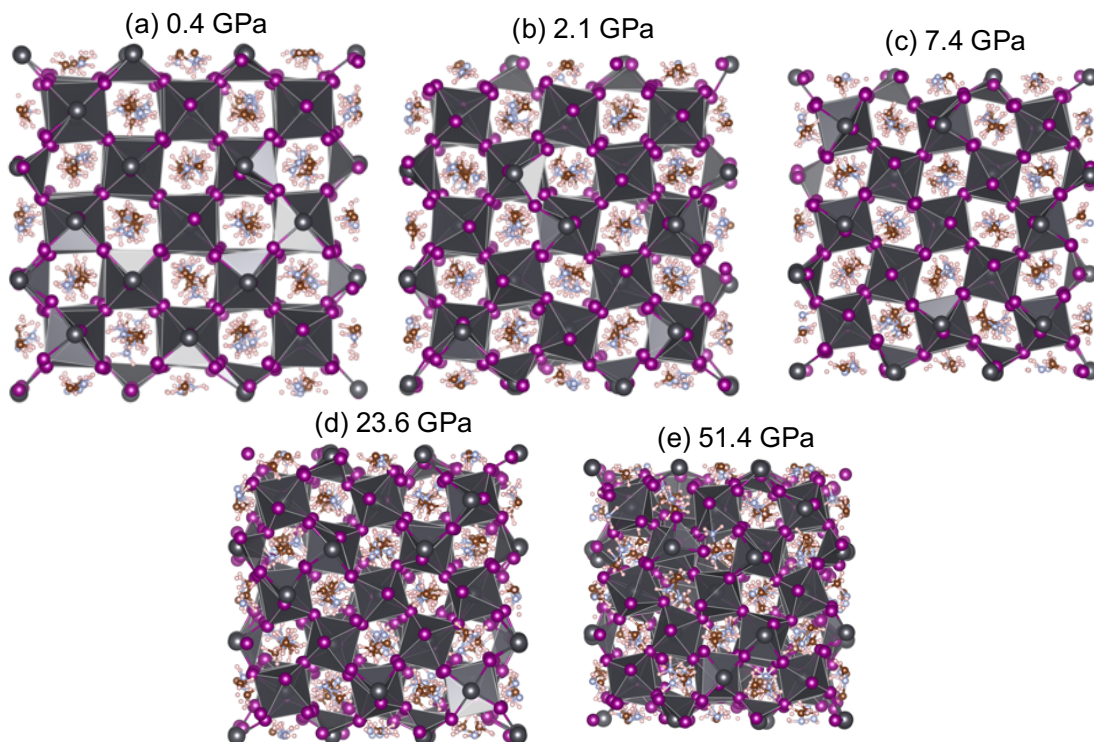


Figure S1. Snapshots of the hybrid perovskite (MAPbI<sub>3</sub>) at various hydrostatic pressures showing the distortions in the octahedral tilts as a result of increasing pressure.

The initial computational domain without hydrostatic pressure are equilibrated under the Nose-Hoover thermostat and barostat,<sup>1</sup> (which is the NPT integration with the number of particles, pressure and temperature of the system held constant) for a total of 1 ns at 0 bar pressure with a time step of 0.5 fs. Following the NPT integration, an NVT integration (with constant volume and number of particles) is implemented to equilibrate the hybrid perovskite structure at the desired temperature of 300 K. Periodic boundary conditions are applied in all directions for all the simulations. After the system is equilibrated hydrostatic pressure is applied along the three principle directions and NPT integration is applied for another 1 ns. Figure S1 shows examples of the hybrid perovskite structures at different pressures highlighting the severe octahedral tilts that arise due to the application of increasing pressure.

After equilibration, the thermal conductivities of the hybrid perovskites at different hydrostatic pressures is predicted via the Green-Kubo (GK) approach under the equilibrium molecular dynamics (EMD) framework. In this formalism, the thermal conductivities along the three principle directions are calculated as,

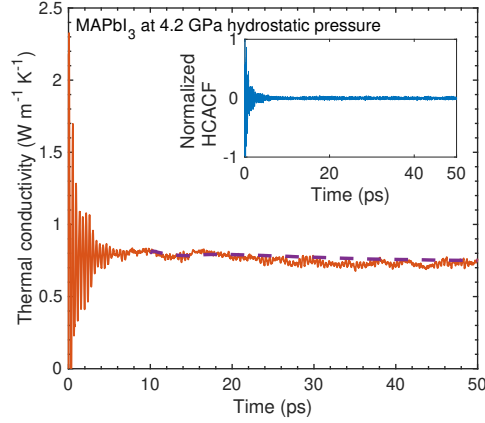


Figure S2. Green-Kubo predicted thermal conductivity of MAPbI<sub>3</sub> as a function of the integration time. (inset) HCACF vs. time for MAPbI<sub>3</sub> crystal showing that the integration time of 50 ps is enough to provide a converged thermal conductivity.

$$\kappa_{x,y,z} = \frac{1}{k_B V T^2} \int_0^\infty \langle J_{x,y,z}(t) J_{x,y,z}(0) \rangle dt. \quad (1)$$

where,  $t$  is time,  $T$  and  $V$  are the temperature and volume of the systems, respectively, and  $\langle J_{x,y,z}(t) J_{x,y,z}(0) \rangle$  is the component of the heat current autocorrelation function (HCACF) in the prescribed direction and is given as,

$$\mathbf{J} = \frac{1}{V} \left( \sum_i \mathbf{v}_i \epsilon_i + \sum_i \mathbf{S}_i \cdot \mathbf{v}_i \right), \quad (2)$$

where,  $\mathbf{v}_i$ ,  $\epsilon_i$  and  $\mathbf{S}_i$  are the velocity, energy and stress of atom  $i$ .

To ensure that the HCACF decays to zero, we set the total correlation time period for the integration of the HCACF to 50 ps as shown in the inset of Fig. S2. The heat current is computed every 10 time steps during the data collection period followed by integration of the heat current to calculate the converged thermal conductivity for the hybrid perovskites. The converged thermal conductivity is determined from the integration from 10 ps to 50 ps as shown in Fig. S2 (dashed line) and the uncertainties in the EMD calculations are determined from ten independent simulations and averaging the thermal conductivity from 10 to 50 ps correlation time. The uncertainties ranged from 8 to 11 % as exemplified in Figs. S4a and S4b showing distribution of thermal conductivities of MAPbI<sub>3</sub> at 0 GPa (with  $\kappa=0.52\pm0.04$  W m<sup>-1</sup> K<sup>-1</sup>) and 40 GPa (with  $\kappa=3.21\pm0.36$  W m<sup>-1</sup> K<sup>-1</sup>), respectively. The normal distribution fits with the same average thermal conductivities and uncertainties are also shown.

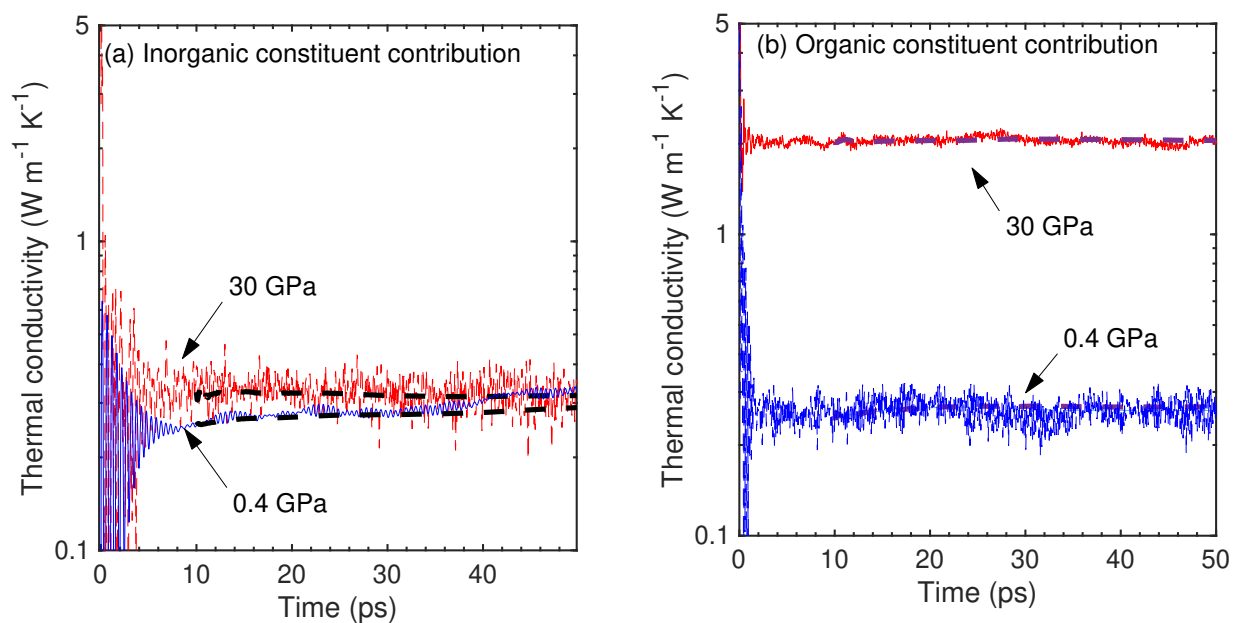


Figure S3. Separate contributions from the (a) inorganic and (b) organic constituents to the total thermal conductivity for two cases of low (0.4 GPa) and high (30 GPa) hydrostatic pressures.

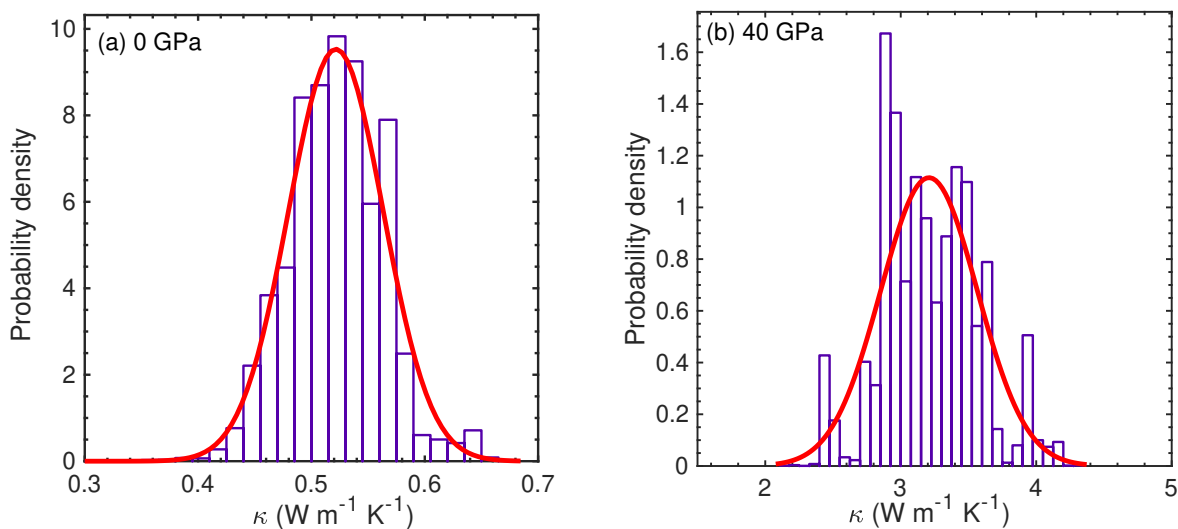


Figure S4. Distributions of thermal conductivities of MAPbI<sub>3</sub> from 10 independent simulations under (a) 0 GPa ( $\kappa=0.52\pm0.04 \text{ W m}^{-1} \text{K}^{-1}$ ) and (b) 40 GPa ( $\kappa=3.21\pm0.36 \text{ W m}^{-1} \text{K}^{-1}$ ) hydrostatic pressures. The red curves represent the normal distribution fits with the average thermal conductivities and uncertainties.

Table S1. Thermal conductivities at 300 K, 350 K and 400 K for MAPbI<sub>3</sub> at three different hydrostatic pressures. The pressure increase leads to similar enhancements (within uncertainties) of thermal conductivity for the three different temperatures.

Temperature (K)	$\kappa$ @ 0 GPa (W m <sup>-1</sup> K <sup>-1</sup> )	$\kappa$ @ 7.4 GPa (W m <sup>-1</sup> K <sup>-1</sup> )	$\kappa$ @ 20 GPa (W m <sup>-1</sup> K <sup>-1</sup> )	$\kappa$ @ 45 GPa (W m <sup>-1</sup> K <sup>-1</sup> )
300	0.52±0.04	1.19±0.13	2.13±0.23	3.69±0.41
350	0.55±0.05	1.15±0.11	2.07±0.23	3.52±0.39
400	0.53±0.05	1.21±0.11	1.99±0.22	3.41±0.37

The contributions from each atom in the simulation domain to the total heat flux can be calculated with Eq. 2 and the contributions to thermal conductivity from the inorganic and organic constituents can be easily separated. This is shown in Fig. S3 for low (0.4 GPa) and high (30 GPa) hydrostatic pressures, where Fig. S3a shows the contribution from the inorganic part, Fig. S3b shows the contributions from the organic part.

Although the EMD approach has been extensively used to predict thermal conductivity of different crystalline and disordered systems,<sup>2-10</sup> there has been some recent work in literature that speculate the accuracy of thermal conductivity predictions via Eq. 1 due to uncertainties associated with finite domain sizes.<sup>3,5,8,11-15</sup> To ensure that the GK-predicted thermal conductivities are not influenced by size effects for the hybrid perovskite, the length of the simulation box ( $d$ ) are chosen to produce converged values of thermal conductivities as shown in Fig S6 for two different pressures at low (0.4 GPa) an high (27 GPa) hydrostatic pressures as a function of  $d$ . The convergence of thermal conductivities within the uncertainties suggest that no size effects are prevalent in the GK predictions.

Thermal conductivity predictions using the GK approach for three different temperatures and four different pressures are shown in Table S1. The enhancement in thermal conductivity due to hydrostatic pressures is observed for all three temperatures considered, which validates the pressure dependent thermal conductivities calculated at 300 K (as shown in Fig. 1c of the main manuscript). The thermal conductivities are similar within uncertainties for the 300 K to 400 K temperature range, which is in-line with prior GK results by Wang *et al.*<sup>16</sup> Note, also consistent with Wang *et al.*,<sup>16</sup> the thermal conductivity increases at lower temperatures due to decrease in anharmonic phonon scattering processes as shown in Fig. S5.

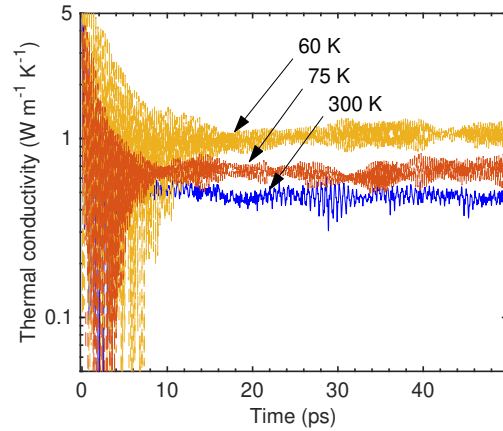


Figure S5. Green Kubo-predicted thermal conductivity of  $\text{MAPbI}_3$  at different temperatures. As temperature is increased, the thermal conductivity decreases due to higher anharmonic scattering.

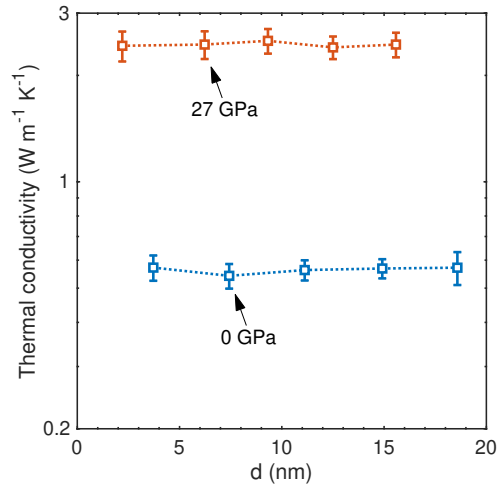


Figure S6. Size independent thermal conductivities calculated via the GK approach for low (0.4 GPa) and high (27 GPa) hydrostatic pressures.

The implementation of the predefined calculations for the virial stress tensor while computing the heat flux to predict the thermal conductivity of systems with many-body interatomic potentials in LAMMPS has been a subject of considerable contention in recent years.<sup>17–19</sup> Therefore, to verify the EMD results, additional approach-to-nonequilibrium MD (AEMD) and nonequilibrium MD (NEMD) simulations are carried out to gain more confidence in the GK-predicted thermal conductivity (that utilizes the heat flux calculations in LAMMPS) for the  $\text{MAPbI}_3$  computational domain. For the AEMD calculations, the simulation domains (with varying lengths from 10 nm

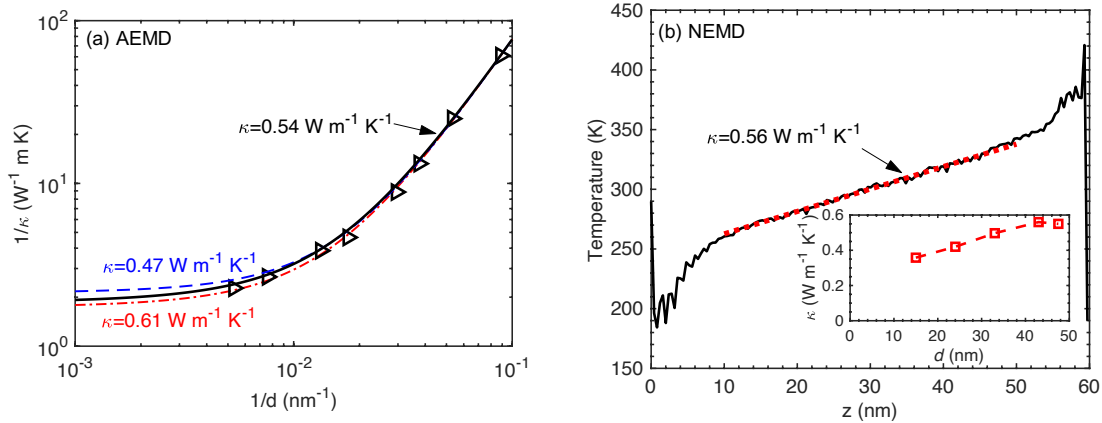


Figure S7. Inverse of thermal conductivity,  $1/\kappa$ , as a function of the inverse of the computational domain length,  $1/d$ , calculated via the approach-to-equilibrium method. Extrapolating to  $1/d = 0$  predicts the size-independent thermal conductivity of  $0.54 \text{ W m}^{-1} \text{ K}^{-1}$  for the  $\text{MAPbI}_3$  computational domain. The dashed-lines represent the 95% confidence bounds for the extrapolation to  $1/d=0$ . (b) Nonequilibrium molecular dynamics simulation of  $\text{MAPbI}_3$  with a computational domain size of  $2.5 \times 2.5 \times 60 \text{ nm}^3$ . Invoking Fourier’s law, the thermal conductivity of  $\text{MAPbI}_3$  is predicted to be  $\sim 0.56 \text{ W m}^{-1} \text{ K}^{-1}$ . (inset) NEMD-predicted thermal conductivity as a function of  $d$ .

to 190 nm in the  $z$ -direction) are divided into equal halves in the specified direction and a step-like temperature profile is created in the prescribed direction.<sup>20,21</sup> The systems are then evolved in a microcanonical ensemble and the thermal conductivities are extracted by relating the time evolution of the temperature profile to the thermal diffusivity of the material; further details of the AEMD approach can be found in Ref. 20. As considerable size effects can influence the AEMD results,<sup>20,22</sup> the ‘bulk’ thermal conductivity of  $\text{MAPbI}_3$  according to the AEMD approach is calculated from the inverse of thermal conductivity,  $1/\kappa$ , plotted as a function of the inverse of the computational domain length,  $1/d$ , and extrapolated to  $1/d = 0$  to predict the size-independent thermal conductivity as shown in Fig. S7a. This approach predicts a thermal conductivity of  $\sim 0.54 \text{ W m}^{-1} \text{ K}^{-1}$ , which agrees with our GK-predicted thermal conductivity providing confidence in our GK approach to correctly predict the thermal conductivity for  $\text{MAPbI}_3$ .

To further validate the GK predictions, additional NEMD simulations with varying  $d$  in the 10 nm to 60 nm range are conducted. For the NEMD simulations, a steady-state temperature gradient is established by adding and subtracting equal amounts of energies from hot and cold baths placed

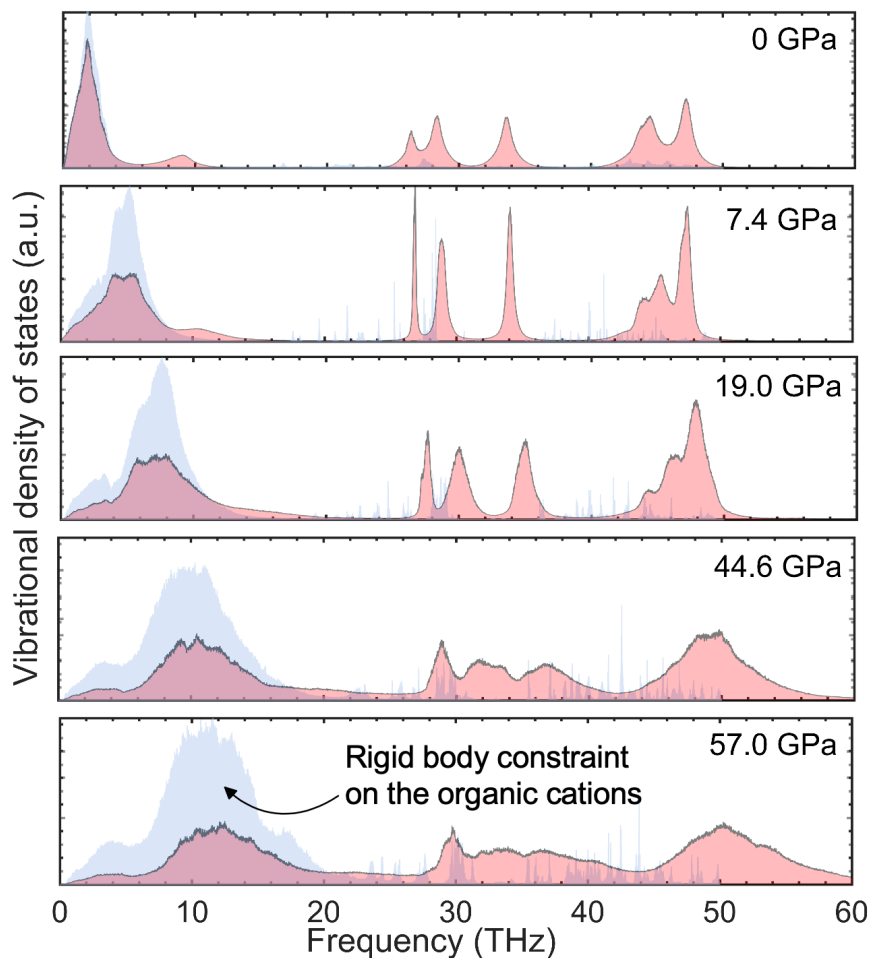


Figure S8. Vibrational density of states computed from the Fourier transform of the autocorrelation of the velocities of the atoms in the MAPbI<sub>3</sub> computational domain for the organic constituents at different pressures showing the hardening of the vibrations in both constituents as the pressure is increased. For comparison, calculations are also performed with a rigid body constraint applied to the organic molecules as shown by the blue shaded region.

at each ends of the computational domain. A fixed wall at either side of the domain is enforced for our NEMD simulations. The temperature profile along the direction of the applied temperature gradient is obtained by averaging the temperature of the atoms along equally spaced bins for a total of 10 ns. The thermal conductivity is predicted via Fourier's law by ignoring the initial 3 ns of data to create time-averaged steady-state temperature profiles as shown in Fig. S7b. For longer simulation cell lengths (>45 nm) along the applied heat flux direction, the thermal conductivity converges to  $\sim 0.56 \text{ W m}^{-1} \text{ K}^{-1}$ , which agrees with the AEMD predictions and the predictions

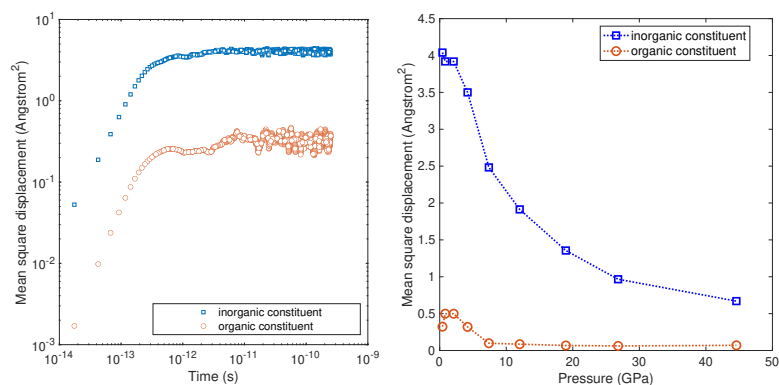


Figure S9. (a) Calculations of mean-squared displacements (MSD) of inorganic and organic constituents as a function of simulation time. (b) The application of hydrostatic pressure is shown to reduce the (MSD) of both the inorganic and organic components.

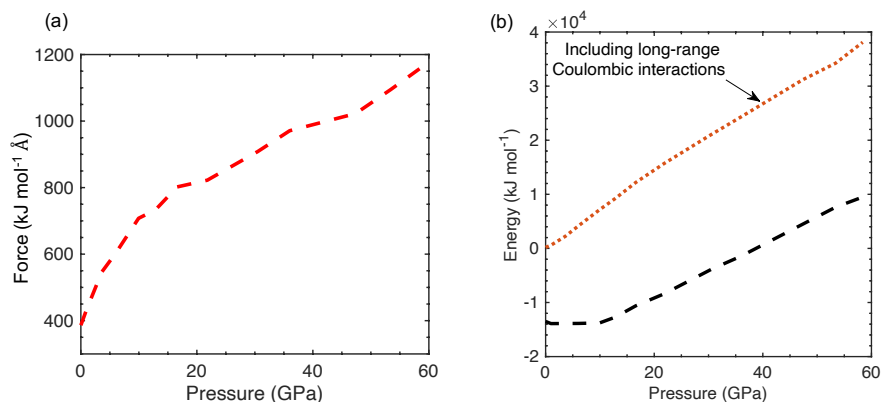


Figure S10. (a) Force between Pb and I atoms as a function of applied hydrostatic pressure. (b) Interaction energy between the organic cation and the inorganic framework as a function of applied hydrostatic pressure. The dotted line corresponds to the interaction energy calculated by considering the long-range Coulombic energy while the dashed line corresponds to calculations with only the pairwise energy between the organic and inorganic constituents.

from the GK approach.

The vibrational density of states (DOS) from the MD simulations are calculated by outputting the velocities of the atoms every 10 time steps for a total of 1 ns. Subsequently, a velocity autocorrelation function algorithm is used to obtain the local vibrational DOS of the organic and inorganic

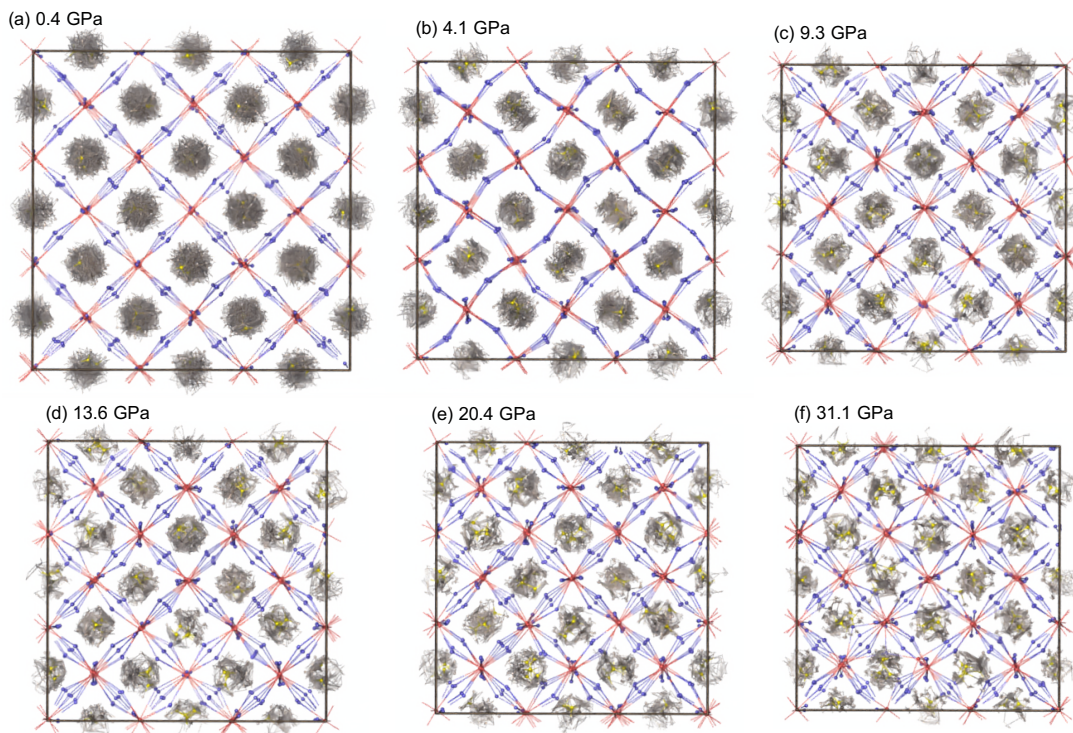


Figure S11. Trajectories calculated for the cations for a total of 50 ps at various hydrostatic pressure conditions.

constituents separately. More specifically, the density of states,  $D(\omega)$ , is obtained from the fourier transform ( $\mathcal{F}$ ) of the velocity correlation function (VACF)<sup>2</sup> by the Welch method of power spectral density estimation and is normalized as follows,

$$D(\omega) = \frac{1}{2} m \mathcal{F}(VACF) \frac{1}{k_B T} \rho \quad (3)$$

where  $m$  is the atomic mass of the different species,  $k_B$  is the Boltzmann constant,  $T$  is the local temperature, and  $\rho$  is the atomic density. The DOS calculated for the organic cations for the various hydrostatic pressure conditions studied in this work is shown in Fig. S8. Also included in the figure are the calculations performed with a rigid body constraint applied to the organic molecules as shown by the blue shaded region. The low energy vibrations are preserved while the intramolecular vibrations disappear due to the rigid body constraint. Similar to that of the organic cations with the full degrees of freedom, the application of pressure broadens the low energy peak for the rigid body case.

Calculations of mean-squared displacements (MSD) of atoms in the computational domains are also performed to investigate their dynamics as hydrostatic pressures are increased. The MSDs as

a function of simulation time for the inorganic and organic constituents are shown in Fig. S9a and the MSDs as a function of pressure for the two constituents are shown in Fig. S9b. The application of pressure restricts the motion of the two species and lowers their MSD.

## REFERENCES

- <sup>1</sup>W. G. Hoover, *Phys. Rev. A* **31**, 1695 (1985).
- <sup>2</sup>M. P. Allen and D. J. Tildesley, *Computer simulation of liquids (Oxford Science Publications)*, reprint ed., Oxford science publications (Oxford University Press, 1989).
- <sup>3</sup>P. K. Schelling, S. R. Phillpot, and P. Keblinski, *Phys. Rev. B* **65**, 144306 (2002).
- <sup>4</sup>A. McGaughey and M. Kaviany, *International Journal of Heat and Mass Transfer* **47**, 1799 (2004).
- <sup>5</sup>A. McGaughey and M. Kaviany, *International Journal of Heat and Mass Transfer* **47**, 1783 (2004).
- <sup>6</sup>A. Henry and G. Chen, *Phys. Rev. Lett.* **101**, 235502 (2008).
- <sup>7</sup>A. S. Henry and G. Chen, *Journal of Computational and Theoretical Nanoscience* **5**, 141 (2008).
- <sup>8</sup>Z. Wang, S. Safarkhani, G. Lin, and X. Ruan, *International Journal of Heat and Mass Transfer* **112**, 267 (2017).
- <sup>9</sup>W. Lv and A. Henry, *New Journal of Physics* **18**, 013028 (2016).
- <sup>10</sup>Y. Chalopin, K. Esfarjani, A. Henry, S. Volz, and G. Chen, *Phys. Rev. B* **85**, 195302 (2012).
- <sup>11</sup>J. Che, T. Çağın, W. Deng, and W. A. G. III, *The Journal of Chemical Physics* **113**, 6888 (2000), <http://dx.doi.org/10.1063/1.1310223>.
- <sup>12</sup>J. Chen, G. Zhang, and B. Li, *Physics Letters A* **374**, 2392 (2010).
- <sup>13</sup>S. G. Volz and G. Chen, *Phys. Rev. B* **61**, 2651 (2000).
- <sup>14</sup>H. Dong, Z. Fan, L. Shi, A. Harju, and T. Ala-Nissila, *Phys. Rev. B* **97**, 094305 (2018).
- <sup>15</sup>L. Sun and J. Y. Murthy, *Applied Physics Letters* **89**, 171919 (2006), <https://doi.org/10.1063/1.2364062>.
- <sup>16</sup>M. Wang and S. Lin, *Advanced Functional Materials* **26**, 5297 (2016), <https://onlinelibrary.wiley.com/doi/pdf/10.1002/adfm.201600284>.
- <sup>17</sup>Z. Fan, L. F. C. Pereira, H.-Q. Wang, J.-C. Zheng, D. Donadio, and A. Harju, *Phys. Rev. B* **92**, 094301 (2015).
- <sup>18</sup>P. Boone, H. Babaei, and C. E. Wilmer, *Journal of Chemical Theory and Computation*, Journal

of Chemical Theory and Computation **15**, 5579 (2019).

<sup>19</sup>D. Surblys, H. Matsubara, G. Kikugawa, and T. Ohara, Phys. Rev. E **99**, 051301 (2019).

<sup>20</sup>K. R. Hahn, M. Puligheddu, and L. Colombo, Phys. Rev. B **91**, 195313 (2015).

<sup>21</sup>C. Caddeo, C. Melis, M. I. Saba, A. Filippetti, L. Colombo, and A. Mattoni, Phys. Chem. Chem. Phys. **18**, 24318 (2016).

<sup>22</sup>E. Lampin, P. L. Palla, P.-A. Francioso, and F. Cleri, Journal of Applied Physics **114**, 033525 (2013), <https://doi.org/10.1063/1.4815945>.